

The electronic structure of intrinsic magnetic topological insulator MnBi_2Te_4 quantum wires

Zhu-Cai Yin,¹ Jian Li,^{1,2,*} Qing-Xv Li,^{1,2} and Jia-Ji Zhu^{1,2,†}

¹*School of Science and Laboratory of Quantum Information Technology,
Chongqing University of Posts and Telecommunications, Chongqing 400065, China*

²*Institute for Advanced Sciences, Chongqing University of Posts and Telecommunications, Chongqing 400065, China*
(Dated: March 14, 2023)

The ferromagnetic and antiferromagnetic nanostructure are crucial for fundamental spintronics devices, motivated by its potential application in spintronics, we theoretically investigate the electronic structure of the ferromagnetic and antiferromagnetic phases of the cylindrical intrinsically magnetic topological insulator MnBi_2Te_4 quantum wires for both cases. We demonstrate that a few surface states exist between the bulk band gap in the ferromagnetic phase, with only one spin branch. In the antiferromagnetic phase, we show that three coexistent states exist between the energy gaps of the quantum wires.

I. INTRODUCTION

The continuous progress in molecular beam epitaxial growth and etching techniques offers today unprecedented possibilities to fabricate isolated semiconductor heterostructures, which exhibit quantum confinement of charge carriers in two and three spatial dimensions¹⁻³. The momentum-space confined electrons and holes are zero-dimensional (0D) for quantum dots (QDs) and one-dimensional (1D) for quantum wires (QWRs)^{4,5}, displaying a broad range of rich mechanics behavior. Various semiempirical methods such as $\mathbf{k} \cdot \mathbf{p}$ theory, density-functional theory, and tight-binding method have been used to calculate the electronic structure of conventional semiconductor QWRs, which are essential to determine the physical properties of such systems accurately. Due to the unique 1D structure, the electron can move freely only in one direction, and its density of states are concentrated in a few peaks, which means that QWRs can be used for a complementary-metal-oxide-semiconductor field-effect transistor⁶, field-effect transistors⁷, single-electron transistors⁸. In addition, the QWRs also opens new opportunities for realizing high-efficiency photovoltaic devices for its remarkable optical properties⁹.

Conventional semiconductor QWRs are still at its experimental stage, so many different types of QWRs were proposed to expand their application, including superconductor QWRs¹⁰, metal QWRs¹¹, insulator QWRs^{12,13}, and topological insulator (TI) QWRs^{14,15}. Among them, Bi_2Se_3 topological insulator and Cr doped Bi_2Se_3 magnetic topological insulators (MTI) are both layered chalcogenide semiconductors, which can be prepared by melting and annealing methods, the structural modulation QWRs can be introduced by etching a QW sample. The Bi_2Se_3 QWRs exhibit robust topological surface states, which provide a good platform for studying ballistic transport, and it's persistent charge current and spin current can be induced by driven magnetic flux¹⁵. For MTI in the quantum anomalous Hall state, MTI/superconductor QWRs have extensive stability regions for both topological and nontopological states, facilitating the creation and manipulation of Majorana particles on the MTI surface¹⁶, the quasi 1D quantum anomalous Hall structures can be fabricated for a scalable protocol for quantum computation¹⁷, along with possibly pave the way for experimental realizations of helical

states in magnetically doped QWRs, which have been demonstrated to be auspicious materials for future nanoelectronics and spintronics¹⁸.

However, MTI created utilizing randomly distributed magnetic dopants leads to strongly inhomogeneous magnetic and electronic properties of these materials, restricting its applications in spintronics. In 2019, *M.M.Otrokov et al.* found that layered van der Waals compound MnBi_2Te_4 is an intrinsic magnetic topological insulator¹⁹, which comprises seven-atom layers (e.g., Te-Bi-Te-Mn-Te-Bi-Te) arranged along the z direction, known as a septuple-layer (SL) blocks, and the blocks bound to each other by van der Waals forces (FIG. 1 (a)).

The spins of Mn-Mn are ferromagnetic-coupled (FM) in each SL, but antiferromagnetic-coupled (AFM) with each other along the z direction, then forming 3D A-type AFM in their van der Waals layered bulk²⁰. More interestingly, atomically thin MnBi_2Te_4 has been demonstrated that FM (AFM) when the samples have an odd (even) number of septuple layers, and shows zero-field quantum anomalous Hall (intrinsic axion insulators) states²¹⁻²³. In addition, the quantum confinement effect will make the system to be more interesting, but no such nanostructure has been well studied.

In this work, we focus on the distinguishing features of the single electron energy spectrum of cylindrical FM and AFM phases MnBi_2Te_4 QWRs separately, which is a key to understanding the few electron features and charge-transport properties in these systems. For the FM phase, we predict a surface state with spin-degeneracy is disrupted by intrinsic magnetic properties that exist between the bulk band gap, in contrast to TI QWRs. For the AFM phase, Our numerical results demonstrate that three subbands exist between the bulk band gap of the MnBi_2Te_4 QWRs, and characterized by the coexistent states (combination states which coexisting surface states near the boundary and centre states near the center of the QWRs).

II. MODEL AND METHOD

We consider a cylindrical MnBi_2Te_4 QWRs schematically shown in FIG. 1(c), the low-energy properties of MnBi_2Te_4 QWRs near the Γ point can be well described by a four-band effective Hamiltonian²⁴ with a lateral confinement in the basis

$|P1_z^+, \uparrow\rangle, |P2_z^-, \uparrow\rangle, |P1_z^+, \downarrow\rangle$ and $|P2_z^-, \downarrow\rangle$. Here the superscripts “+”, “-” stand for the parity of the corresponding states, P denotes the p -like orbital states of the atoms, 1(2) stands for Bi(Te) atoms and \uparrow (\downarrow) is the spin-up (spin-down) state, respectively.

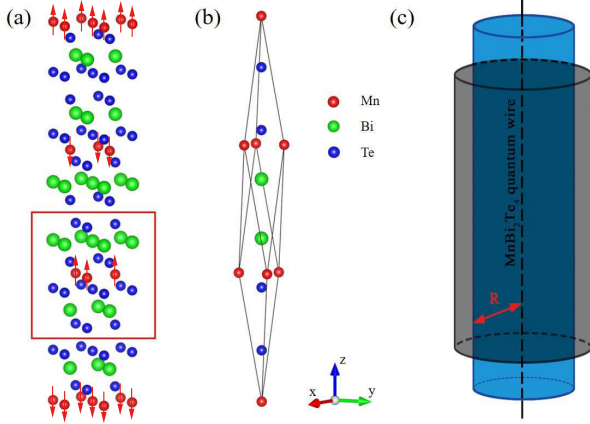


FIG. 1: (Color online) (a) Crystal structure of MnBi₂Te₄, the seven-layer stacked structure of Ti-Bi-Te-Mn-Te-Bi-Te is shown in the red box, and the red arrows represent the spin moment of Mn atom. (b) Schematic diagram of paramagnetic rhombohedral unit cell of bulk MnBi₂Te₄. (c) Schematic diagram of MnBi₂Te₄ QWRs aligned along the z -axis, R is the radius of the QWRs.

It has been proposed that the magnetic ground state of MnBi₂Te₄ is an AFM topological insulator state, while its magnetic states can be tunable from AFM to FM under the external magnetic fields. Therefore, we investigate the physical properties for both FM and AFM phases MnBi₂Te₄ QWRs. The etching introduces a sharp confinement potential $V(\rho)$ along the radial direction of the QWRs, for simplicity, we take $V(\rho)$ as a cylindrical hard wall potential $V(\rho) = 0$ for $\rho < R$ and $V(\rho) = \infty$ for $\rho > R$. The low energy effective Hamiltonian of FM MnBi₂Te₄ QWRs is

$$H_{FM}^{QWRs}(k) = H_N(k) + \delta H_{FM}(k) + V(\rho), \quad (1)$$

where $H_N(k)$ is the nonmagnetic state Hamiltonian:

$$H_N(k) = \varepsilon_0(k) + \begin{pmatrix} M_\gamma(k) & A_1 k_z & 0 & A_2 k_- \\ A_1 k_z & -M_\gamma(k) & A_2 k_- & 0 \\ 0 & A_2 k_+ & M_\gamma(k) & -A_1 k_z \\ A_2 k_+ & 0 & -A_1 k_z & -M_\gamma(k) \end{pmatrix}, \quad (2)$$

where, $k_\pm = k_x \pm ik_y$, $\varepsilon_0(k) = C + D_1 k_z^2 + D_2 (k_x^2 + k_y^2)$, $M_\gamma(k) = M_0^\gamma + B_1^\gamma k_z^2 + B_2^\gamma (k_x^2 + k_y^2)$, the band parameters is taken from Ref. [24]: $C = 0.0539$ eV, $D_1 = -4.0339$ eVÅ², $D_2 = 4.4250$ eVÅ², $A_1 = 1.3658$ eVÅ, $A_2 = 1.9985$ eVÅ, $M_0^\gamma = 0.0307$ eV, $B_1^\gamma = 4.2857$ eVÅ², $B_2^\gamma = 8.3750$ eVÅ². And $\delta H_{FM}(k)$ is the FM perturbative term given by:

$$\delta H_{FM}(k) = \begin{pmatrix} M_1(k) & A_3 k_z & 0 & A_4 k_- \\ A_3 k_z & M_2(k) & -A_4 k_- & 0 \\ 0 & -A_4 k_+ & -M_1(k) & A_3 k_z \\ A_4 k_+ & 0 & A_3 k_z & -M_2(k) \end{pmatrix}, \quad (3)$$

where, $M_{1,2}(k) = M_\alpha(k) \pm M_\beta(k)$ characterize the Zeeman coupling with the magnetized Mn orbitals, and $M_j(k) = M_0^j + B_1^j k_z^2 + B_2^j (k_x^2 + k_y^2)$, where $j = \alpha, \beta$. The band parameters is also taken from Ref. [24]: $A_3 = -0.5450$ eVÅ, $A_4 = 1.1384$ eVÅ, $M_0^\alpha = -0.1078$ eV, $B_1^\alpha = 0.6232$ eVÅ², $B_2^\alpha = 0.6964$ eVÅ², $M_0^\beta = -0.0880$ eV, $B_1^\beta = 2.7678$ eVÅ², $B_2^\beta = 1.9650$ eVÅ².

For the AFM phase MnBi₂Te₄ QWRs, the effective Hamiltonian is

$$H_{AFM}^{QWRs}(k) = H_{AFM}(k) + V(\rho) \quad (4)$$

where

$$H_{AFM}(k) = \varepsilon'_0(k) + \begin{pmatrix} M'(k) & A'_1 k_z & 0 & A'_2 k_- \\ A'_1 k_z & -M'_\gamma(k) & A'_2 k_- & 0 \\ 0 & A'_2 k_+ & M'_\gamma(k) & -A'_1 k_z \\ A'_2 k_+ & 0 & -A'_1 k_z & -M'_\gamma(k) \end{pmatrix}, \quad (5)$$

the Hamiltonian of $H_{AFM}(k)$ is the same as that of the non-magnetic form $H_N(k)$, i.e. $\varepsilon'_0(k) = C' + D'_1 k_z^2 + D'_2 (k_x^2 + k_y^2)$, $M'(k) = M'_0 + B'_1 k_z^2 + B'_2 (k_x^2 + k_y^2)$, but with different band parameters²⁴, $C' = -0.0048$ eV, $D'_1 = 2.7232$ eVÅ², $D'_2 = 17.0000$ eVÅ², $A'_1 = 2.7023$ eVÅ, $A'_2 = 3.1964$ eVÅ, $M'_0 = -0.1165$ eV, $B'_1 = 11.9048$ eVÅ², $B'_2 = 9.4048$ eVÅ².

The single electron states and the corresponding eigenstates of the QWRs are obtained from the Schrödinger equation

$$H_{FM/AFM}^{QWRs}(k) |\Psi(k)\rangle = E_{FM/AFM}^k |\Psi(k)\rangle, \quad (6)$$

which can be obtained numerically by expanding the wave function in terms of the first kind of the cylindrical Bessel basis²⁵.

$$|\Psi\rangle = \sum_{n,m} \begin{pmatrix} C_{n,m}^{(1)} \varphi_{n,m} \varphi_z \\ C_{n,m}^{(2)} \varphi_{n,m-1} \varphi_z \\ C_{n,m}^{(3)} \varphi_{n,m} \varphi_z \\ C_{n,m}^{(4)} \varphi_{n,m+1} \varphi_z \end{pmatrix}, \quad (7)$$

where $\varphi_{n,m} = \frac{1}{\sqrt{\pi} R \times J_{m+1}(k_n^m R)} J_m(k_n^m \rho / R) e^{im\theta}$, $\varphi_z = \frac{1}{\sqrt{2\pi}} e^{ik_z z}$, $C_{n,m}^{(i)}$ is the expanding coefficient. The number of eigenstates used in the expansion is chosen to ensure the convergence of the calculated energies of the QWRs within and nearby the bulk gap. $\hat{L}_z = -i\partial/\partial\theta$ is the angular momentum of the envelope function, therefore, $m = \langle \hat{L}_z \rangle = 0, \pm 1, \pm 2, \dots$ is a good quantum number due to the rotational invariance of $H_{FM}^{QWRs}(k)$ (or $H_{AFM}^{QWRs}(k)$) around the z axis, k_n^m is the n th zero point of the first class of m -th order Bessel function $J_m(x)$, k_z is the wavevector along the QWRs direction, i.e., the z axis, and R is the radius of the cylindrical QWRs.

To determine the single electron states, left multiplication ($\varphi_{n',m'}^* \varphi_z^*, \varphi_{n',m'-1}^* \varphi_z^*, \varphi_{n',m'}^* \varphi_z^*, \varphi_{n',m'+1}^* \varphi_z^*$) to the secular equation (6) to obtain the eigenvalue and expanding coefficient $C_{n,m}^{(i)}$ by solving the eigenvalue problem. The basis set $\varphi_{n,m}(\rho, \theta)$ and φ_z obeys the ortho-normalized condition $\int_0^{2\pi} \int_0^R \varphi_{n,m}(\rho, \theta) \varphi_{n',m'}(\rho, \theta) \rho d\rho d\theta = \delta_{n,n'} \delta_{m,m'}$ and $\int_{-\infty}^{\infty} \varphi_z \varphi_z^* dz = \int_{-\infty}^{\infty} \frac{1}{2\pi} e^{i(k_z - k'_z)z} dz = \delta(k_z - k'_z)$.

III. RESULTS AND DISCUSSIONS

In the first subsection, we present the electronic and density of states (DOS) of the cylindrical MnBi_2Te_4 QWRs in its FM phase, which showing surface states exist between the bulk band gap, and the spectra of the surface states show non-degenerate and spin polarization due to broken $\mathcal{T}\mathcal{I}$ symmetry, where \mathcal{T} is the time reversal symmetry, \mathcal{I} is the inversion symmetry.

In the second subsection, we present the electronic and DOS of the cylindrical MnBi_2Te_4 QWRs in its AFM phase, which showing coexistent states between the bulk band gap, and the energy spectrum have two-fold degeneracy because of conservation $\mathcal{T}\mathcal{I}$ symmetry.

A. Ferromagnetic phase

To begin with, we shows the energy spectrum of FM phase of MnBi_2Te_4 QWRs in Fig. 2(a), which have been calculated numerically from the four-band $\mathbf{k} \cdot \mathbf{p}$ model. The surface states display a mini-gap (~ 8 meV) between the up- and down-branches of the surface state subbands [red solid line in Fig. 2(a)], which comes from the quantization of the orbital angular momentum. In addition, the energy spectrum of the surface states is fully spin-polarized.

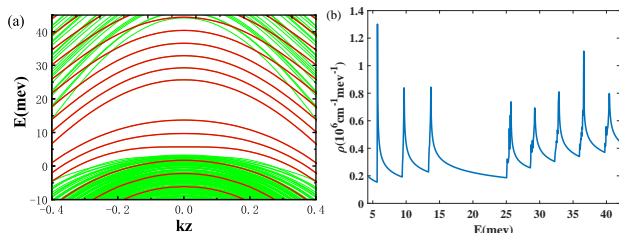


FIG. 2: (Color online) (a) Energy spectrum of the FM MnBi_2Te_4 QWRs with radius $R = 60$ nm, the red solid lines represent the surface states, and green solid lines represent the bulk states. (b) The DOS of the surface states of the QWRs in the bulk band gap.

From the subbands dispersions of the surface states of the QWRs which are shown in Fig. 2(a), one can obtain the DOS per unit length with the following equation:

$$\rho^{1D}(E) = \sum_{i=1}^n \left(\frac{2m^*}{\hbar^2} \right)^{\frac{1}{2}} \frac{1}{\pi(E - E_i)^{\frac{1}{2}}} \Theta(E - E_i), \quad (8)$$

where Θ is the unit step function and the sum over i runs over all the subbands. Fig. 2(b) shows the surface states DOS of the QWRs, the maxima in the DOS at around the subband maxima come from the one-dimensional feature of the surface states subbands, i.e. the charge would be expected to accumulate at around the point.

In Fig. 3, we plot the energy spectra of the surface and bulk states of the FM phase MnBi_2Te_4 QWRs as a function of the angular momentum quantum number m at the center of the Brillouin zone $k_z = 0$. The spectra of the surface states show

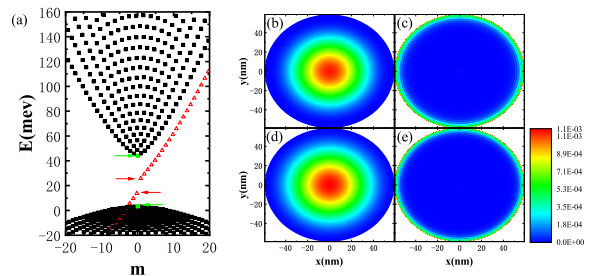


FIG. 3: (Color online) (a) The energy spectrum of a FM phase MnBi_2Te_4 QWRs as a function of the angular momentum quantum number m with radius $R = 60$ nm, and $k_z = 0$. (b) and (d) The density distributions of the lowest conduction band and highest valence band states (marked by green arrows in (a)). (c) and (e) The density distributions of one of the states of the surface states (marked by red arrows in (a)).

fully spin-polarized and approximately obeys the linear dispersion against m in Fig. 3(a). Note that only one spin branch is exist compared to the TI cylindrical QWRs¹⁵ due to broken $\mathcal{T}\mathcal{I}$ symmetry, the spins of electrons that carry electrical current are preferentially oriented along the magnetization direction, which is crucial for spintronics applications.

The density distribution of bulk states for the conduction band and valence band are localized at the center of the QWRs as shown in Fig. 3(b) and 3(d) respectively. In contrast to the bulk states, the surface states show interesting ringlike density distribution in the vicinity of the outer surface of the QWRs, as shown in Fig. 3(c) and 3(e) respectively. When this massless Dirac fermion is confined in a FM phase MnBi_2Te_4 QWRs, its lowest energy modes should be the “whispering gallery” mode, similar to an electron (hole) confined in a TI cylindrical QWRs¹⁵ or QDs²⁶.

B. Antiferromagnetic phase

In the following sections, we turn to dealing with the electronic structure of the AFM phase of the MnBi_2Te_4 QWRs. The energy spectra of the surface and bulk states of the AFM phase MnBi_2Te_4 QWRs as a function of the wavevector k_z is shown in Fig. 4(a), compared to the FM phase MnBi_2Te_4 QWRs, the subbands [red and blue solid line in Fig. 4(a)] between the bulk band gap are no longer purely surface states, but coexistent states. Similar to the FM form, one can also obtain the DOS per unit length of AFM phase MnBi_2Te_4 QWRs [see Fig. 4(b)], while the maxima in the DOS at around the subbands maxima come from the one-dimensional feature of the coexistent states subbands, larger DOS comes from the spin degenerate compared to the FM phase MnBi_2Te_4 QWRs, the strong peak near the maxima in the DOS is due to a flatness of the subbands.

To further clarify the electronic states of the AFM phase MnBi_2Te_4 QWRs, we provided its energy spectra of the coexistent states and bulk states as a function of the angular momentum quantum number m at the center of the Brillouin zone

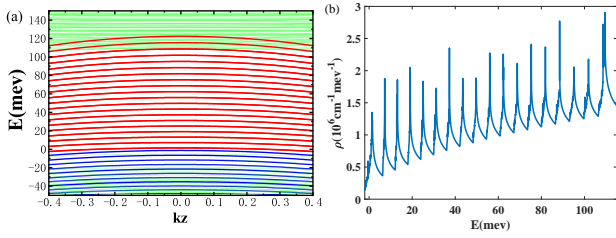


FIG. 4: (Color online) (a) Energy spectrum of the AFM MnBi_2Te_4 QWRs with radius $R = 60$ nm, the red and blue solid lines represent the coexistent states, and green solid lines represent the other states. (b) The DOS of the coexistent states of the QWRs in the bulk band gap.

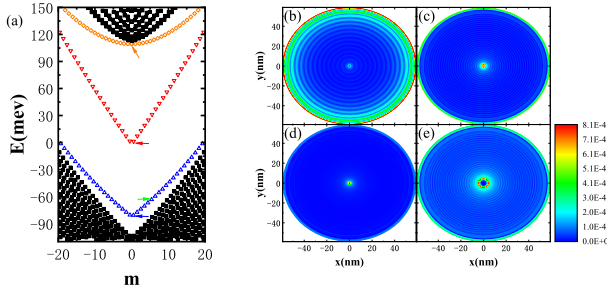


FIG. 5: (Color online) (a) The energy spectrum of a AFM phase MnBi_2Te_4 QWRs as a function of the angular momentum quantum number m with radius $R = 60$ nm, and $k_z = 0$. (b), (c) and (d) The density distributions of the three coexistent states in the band gap (marked by yellow, red and blue arrows in (a) for $m = 0$, separately). (e) The density distributions of the lowest coexistent states in the band gap (marked by green arrows in (a) for $m = 5$).

$k_z = 0$ in Fig. 5(a), one find that three distinct subbands exist between the energy gaps, and the middle of the three subbands obeys the linear dispersion against m , we also given

the density distribution of the three coexistent states between the energy gaps, the density distribution of three distinct subbands states show coexisting surface states near the boundary and centre states near the center of the QWRs, as shown in Fig. 5(b), (c), (d) and (e). Note that although the component of surface states for the lowest branch [marked by blue arrows in Fig. 5(a)] at angular momentum $m = 0$ [see Fig. 5(d)] is not as obvious as a larger m [see Fig. 5(e) $m = 5$ as an example], on the whole, where we approximated call it the coexistent states. The novel coexistent states significantly different from the surface states of the Bi_2Se_3 QWRs and previous FM QWRs, and it can be controlled by tuning the band parameter of D_2' in $\varepsilon_0'(k)$, the kinetic energy of the $\mathbf{k} \cdot \mathbf{p}$ Hamiltonian (5) in our calculation, and thus can be controlled by an external field.

IV. CONCLUSIONS

In summary, we studied the electronic structure for both of the FM and AFM phases MnBi_2Te_4 QWRs. For FM phase QWRs, the numerical results show that surface states exist between the bulk band gap, the spectra of the surface states are fully spin-polarized, and only one spin branch is exists. For AFM phase QWRs, we discovered that three coexistent states exist between the energy gaps, and moreover, the behavior of the coexistent states can be controlled by an external field.

Acknowledgments

This work has been supported by the NSFC (Grant No. 11604036), the Science and Technology Research Program of Chongqing Municipal Education Commission (Grant No. KJQN202000639), and the Scientific Research Program from Science and Technology Bureau of Chongqing City (Grant No. cstc2020jcyj-msxm0925).

* Electronic address: jianli@cqupt.edu.cn

† Electronic address: zhujj@cqupt.edu.cn

¹ R. Ashoori, *Nature* **379**, 413 (1996).

² F. Ansaloni, A. Chatterjee, H. Bohuslavskyi, *et al.*, *Nat. Commun.* **11**, 1 (2020).

³ N. Yazdani, S. Andermatt, M. Yarema, *et al.*, *Nat. Commun.* **11**, 1 (2020).

⁴ S. Heedt, M. Quintero-Pérez, F. Borsoi, *et al.*, *Nat. Commun.* **12**, 1 (2021).

⁵ A. P. Alivisatos, *Science* **271**, 933 (1996).

⁶ R. Böckle, M. Sistani, P. Staudinger, *et al.*, *Nanotechnology* **31**, 445204 (2020).

⁷ R. Ahmad, T. Mahmoudi, M. S. Ahn, *et al.*, *Biosens. Bioelectron.* **100**, 312 (2018).

⁸ C. Thelander, T. Mårtensson, M. T. Björk, *et al.*, *Appl. Phys. Lett.* **83**, 2052 (2003).

⁹ D. Zhang, Q. Zhang, B. Ren, *et al.*, *Nature Photon.* **16**, 284 (2022).

¹⁰ R. Boston, Z. Schnepf, Y. Nemoto, *et al.*, *Science* **344**, 623 (2014).

¹¹ J. Y. Tsai, J. Pan, H. Lin, *et al.*, *Nat. Commun.* **13**, 1 (2022).

¹² J. J. Zhu, K. Chang, R. B. Liu, *et al.*, *Phys. Rev. B* **81**, 113302 (2010).

¹³ S. Vaitiekėnas, Y. Liu, P. Krogstrup, *et al.*, *Nature Phys.* **17**, 43 (2021).

¹⁴ H. F. Legg, D. Loss, and J. Klinovaja, *Phys. Rev. B* **105**, 155413 (2022).

¹⁵ W. K. Lou, F. Cheng, and J. Li, *J. Appl. Phys.* **110**, 093714 (2011).

¹⁶ Y. Zeng, C. Lei, G. Chaudhary, *et al.*, *Phys. Rev. B* **97**, 081102 (2018).

¹⁷ C. Z. Chen, Y. M. Xie, J. Liu, *et al.*, *Phys. Rev. B* **97**, 104504 (2018).

¹⁸ F. Stäbler, A. M. Tselik, and O. M. Yevtushenko, *Phys. Rev. B* **102**, 161102 (2020).

¹⁹ M. Otrokov, I. Klimovskikh, H. Bentmann, *et al.*, *Nature* **576**, 416–422 (2019).

²⁰ M. M. Otrokov, T. V. Menshchikova, M. G. Vergniory, *et al.*, *2D Mater.* **4**, 025082 (2017).

- ²¹ M. M. Otrokov, I. P. Rusinov, M. Blanco-Rey, *et al.*, *Phys. Rev. Lett.* **122**, 107202 (2019).
- ²² J. Li, Y. Li, S. Du, *et al.*, *Sci. Adv.* **5**, eaaw5685 (2019).
- ²³ Y. Deng, Y. Yu, M. Z. Shi, *et al.*, *Science* **367**, 895 (2020).
- ²⁴ D. Zhang, M. Shi, T. Zhu, *et al.*, *Phys. Rev. Lett.* **122**, 206401 (2019).
- ²⁵ J. Li, W. K. Lou, D. Zhang, *et al.*, *Phys. Rev. B* **90**, 115303 (2014).
- ²⁶ K. Chang and W. K. Lou, *Phys. Rev. Lett.* **106**, 206802 (2011).